

Supernova Nucleosynthesis and Extremely Metal-Poor Stars

Nozomu Tominaga¹, Hideyuki Umeda¹, Keiichi Maeda[†],
Nobuyuki Iwamoto¹ and Ken'ichi Nomoto^{1,†}

Department of Astronomy, University of Tokyo, Bunkyo, Tokyo 113-0033, Japan

[†]Institute for the Physics and Mathematics of the Universe, University of Tokyo, Kashiwa, Chiba, 277-8582, Japan

Nuclear Data Center, Nuclear Science and Engineering Directorate, Japan Atomic Energy Agency, Tokai, Ibaraki 319-1195, Japan

Abstract. We investigate hydrodynamical and nucleosynthetic properties of the jet-induced explosion of a population III $40M_{\odot}$ star and compare the abundance patterns of the yields with those of the metal-poor stars. We conclude that (1) the ejection of Fe-peak products and the fallback of unprocessed materials can account for the abundance patterns of the extremely metal-poor (EMP) stars and that (2) the jet-induced explosion with different energy deposition rates can explain the diversity of the abundance patterns of the metal-poor stars. Furthermore, the abundance distribution after the explosion and the angular dependence of the yield are shown for the models with high and low energy deposition rates $\dot{E}_{\text{dep}} = 120 \text{ } 10^{51} \text{ erg s}^{-1}$ and $1.5 \text{ } 10^{51} \text{ erg s}^{-1}$. We also find that the peculiar abundance pattern of a Si-deficient metal-poor star HE 1424-0241 can be reproduced by the angle-delimited yield for $\theta = 30^{\circ} \text{ } 35^{\circ}$ of the model with $\dot{E}_{\text{dep}} = 120 \text{ } 10^{51} \text{ erg s}^{-1}$.

Keywords: Galaxy: halo — gamma rays: bursts — nuclear reactions, nucleosynthesis, abundances — stars: abundances — stars: Population II — supernovae: general

PACS: 26.30.-k, 26.30.Ef, 26.50.+x, 97.10.Tk, 97.20.Tr, 97.20.Wt, 97.60.Bw

INTRODUCTION

In the early universe, the enrichment due to a single supernova (SN) dominates the preexisting metal contents (e.g., [1]). A shock wave compresses the SN ejecta consisting of metals, e.g., C, O, Mg, Si, and Fe, and the circumstellar materials consisting of H and He. The abundance pattern of the enriched gas reflects nucleosynthesis in the SN. The compression will initiate a star formation, called a SN-induced star formation (e.g., [2]); the next-generation stars will be formed from the enriched gases. Thus the abundances of the next-generation stars show a trace of nucleosynthesis in the population (Pop) III SN. The low-mass ($< 1M_{\odot}$) stars among them have long lifetimes, survive until present days, and might be observed as metal-poor stars. Therefore, the metal-poor stars can make a constraint on the nucleosynthesis yield of the Pop III SN.

The abundance patterns of extremely metal-poor (EMP) stars with $[\text{Fe}/\text{H}] < -3$ ¹ suggest that aspherical SN explosions took place in the early universe. The C-enhanced type of the EMP stars has been well explained by a faint SN [3, 4, 5, 6], except for

¹ Here $[A/B] = \log_{10} (N_A/N_B) - \log_{10} (N_A/N_B)_{\odot}$, where the subscript \odot refers to the solar value and N_A and N_B are the abundances of elements A and B, respectively.

TABLE 1. Jet-induced explosion models.

Name	M_0	R_0	\dot{E}_{dep}	E_{dep}	θ_{jet}	Γ_{jet}	f_{th}	$M(\text{Fe})$	M_{rem}
	[M_\odot]	[km]	[$10^{51} \text{ergs s}^{-1}$]	[10^{51}ergs]	[degrees]			[M_\odot]	[M_\odot]
A	1.4	900	120	15	15	100	10^{-3}	2.1×10^{-1}	9.1
B	1.4	900	1.5	15	15	100	10^{-3}	3.9×10^{-6}	16.9

their large Co/Fe and Zn/Fe ratios (e.g., [7, 8]). The enhancement of Co and Zn in low metallicity stars requires explosive nucleosynthesis under high entropy. In a *spherical* model, a high entropy explosion corresponds to a high energy explosion that inevitably synthesizes a large amount of $^{56}\text{Ni}(\text{Fe})$ and leads a bright SN. Thus, it was suggested that some faint SNe were associated with a narrow jet within which a high entropy region is confined [3].

We present hydrodynamical and nucleosynthetic models of the jet-induced explosions of a Pop III $40 M_\odot$ star and show that the jet-induced SN explosions are responsible for the formation of the EMP stars. Further, we investigate the angular dependence of the yield of the jet-induced SNe.

MODELS

We investigate a jet-induced SN explosion of a Pop III $40 M_\odot$ star [3, 6] by means of a two-dimensional relativistic Eulerian hydrodynamic and nucleosynthesis calculation with the gravity [9, 10, 11]. The nucleosynthesis calculation is performed as a post-processing with the reaction network including 280 isotopes up to ^{79}Br ([12, 13], see Table 1 in [3]). The thermodynamic histories are traced by marker particles representing Lagrangian mass elements (e.g., [14, 15]).

The explosion mechanism of gamma-ray burst (GRB)-associated SNe is still under debate (e.g., a neutrino annihilation, [16]; and a magneto-rotation, [17]). Thus, we do not consider how the jet is launched, but we deal the jet parametrically with the following five parameters [11]: energy deposition rate (\dot{E}_{dep}), total deposited energy (E_{dep}), initial half angle of the jets (θ_{jet}), initial Lorentz factor (Γ_{jet}), and the ratio of thermal to total deposited energies (f_{th}).

Jets are injected at a radius $R_0 = 900$ km, corresponding to an enclosed mass of $M_0 = 1.4 M_\odot$, and the jet propagation is followed until a homologously expanding structure is reached ($v \propto r$). Then, the ejected mass elements are identified from whether their radial velocities exceed the escape velocities at their position.

We investigate the dependence of nucleosynthesis outcome on \dot{E}_{dep} for a range of $\dot{E}_{\text{dep},51} = \dot{E}_{\text{dep}}/10^{51} \text{ergs s}^{-1} = 0.3 - 1500$ and in particular show the abundance patterns of the yields of two models; (A) a model with $\dot{E}_{\text{dep},51} = 120$, (B) a model with $\dot{E}_{\text{dep},51} = 1.5$. Here, we fix the other parameters as $E_{\text{dep}} = 1.5 \times 10^{52} \text{ergs}$, $\theta_{\text{jet}} = 15^\circ$, $\Gamma_{\text{jet}} = 100$, and $f_{\text{th}} = 10^{-3}$ in all models. The mass of jets is $M_{\text{jet}} = 8 \times 10^{-5} M_\odot$. The model parameters, the ejected Fe mass [$M(\text{Fe})$], and the central remnant mass (M_{rem}) are summarized in Table 1.

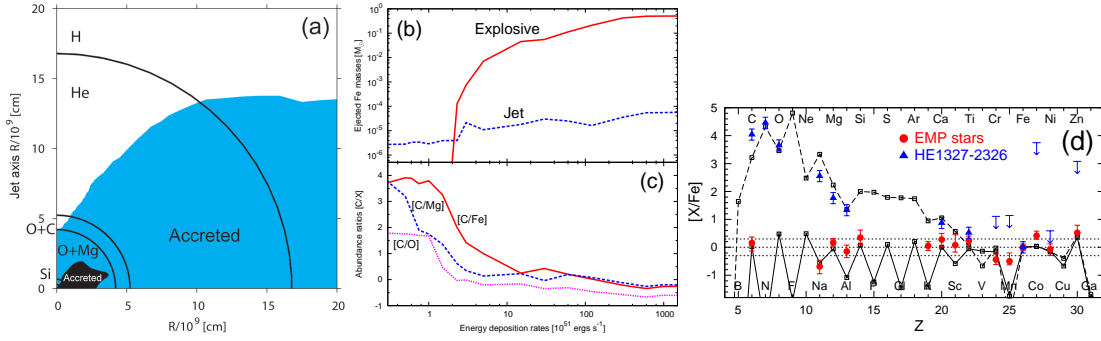


FIGURE 1. (a) Initial locations of the mass elements which are finally accreted for model A (black) and model B (cyan). The circles represent the boundaries between the layers in the progenitor star; the H, He, O+C, O+Mg, and Si layers from the outside. (b) Ejected Fe mass (solid line: explosive nucleosynthesis products, dashed line: the jet contribution) as a function of the energy deposition rate. (c) Dependence of abundance ratios, $[C/Fe]$ (solid line), $[C/Mg]$ (dashed line), and $[C/O]$ (dotted line), on the energy deposition rate. (d) Comparisons of the abundance patterns of metal-poor stars and models. The abundance patterns of the EMP stars ([20], circles) and HE 1327-2326 ([21, 22], triangles) are reproduced by models with $\dot{E}_{\text{dep}51} = 120$ (solid line) and $\dot{E}_{\text{dep}51} = 1.5$ (dashed line).

RESULTS

Fallback

Figure 1a shows “accreted” regions for models A and B, where the accreted mass elements initially located in the progenitor [10, 11]. The O layer is separated into the two layers: (1) the O+Mg layer with $X(^{24}\text{Mg}) > 0.01$ and (2) the O+C layer with $X(^{12}\text{C}) > 0.1$. The inner matter is ejected along the jet-axis but not along the equatorial plane. On the other hand, the outer matter is ejected even along the equatorial plane because the lateral expansion of the shock terminates the infall.

The accreted mass is larger for lower \dot{E}_{dep} . This stems from the balance between the ram pressures of the injecting jet (P_{jet}) and the infalling matter (P_{fall}) (e.g., [18, 19]). The critical energy deposition rate ($\dot{E}_{\text{dep},\text{crit}}$) giving $P_{\text{jet}} = P_{\text{fall}}$ is lower for the outer layer. Thus, the jet injection with lower \dot{E}_{dep} is realized at a later time when the central remnant becomes more massive. Additionally, the lateral expansion of the jet is more efficiently suppressed for lower \dot{E}_{dep} . As a result, the accreted region is larger and M_{rem} is larger for lower \dot{E}_{dep} .

Figures 1b and 1c show the dependence of $M(\text{Fe})$ and the abundance ratios $[C/O]$, $[C/Mg]$, and $[C/Fe]$ on \dot{E}_{dep} , respectively [9, 10]. A model with lower \dot{E}_{dep} has larger M_{rem} , higher $[C/O]$, $[C/Mg]$, and $[C/Fe]$, and smaller $M(\text{Fe})$ because of the larger amount of fallback (Fig. 1a). The larger amount of fallback decreases the ejected mass of the inner core (e.g., Fe, Mg, and O) relative to the ejected mass of the outer layer (e.g., C, Fig. 1a). Since O and Mg are synthesized in the inner layers than C, $[C/O]$ and $[C/Mg]$ are larger for the larger infall of the O layer. Also, the fallback of the O layer decreases $M(\text{Fe})$ because Fe is mainly synthesized explosively in the Si and O+Mg layers. Therefore, the variation of \dot{E}_{dep} in the jet-induced SN explosions predicts that the

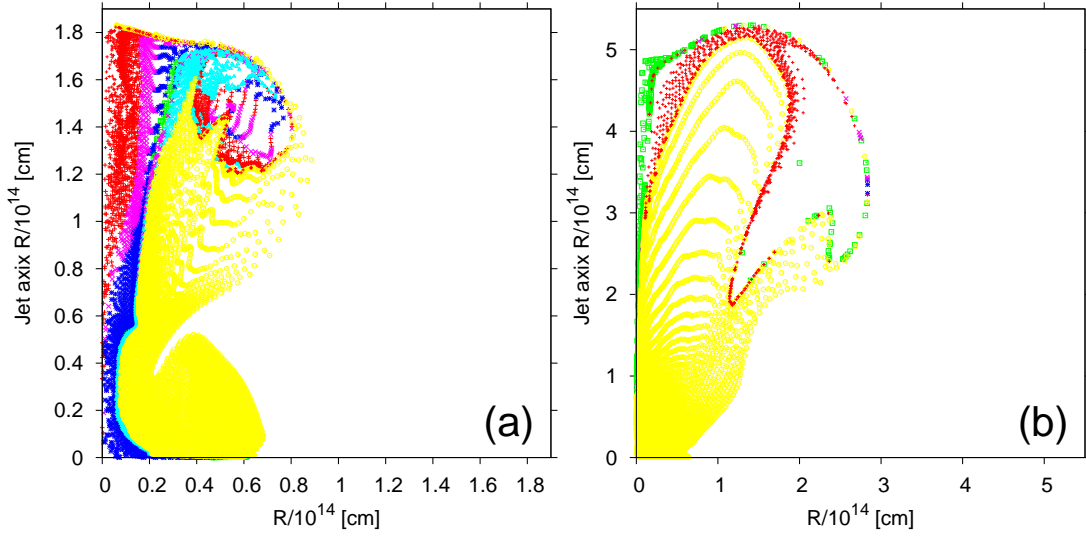


FIGURE 2. Positions of the mass elements at $t = 10^5$ s for (a) model A and (b) model B. Symbols of the marks represents the abundance of the mass element (H: *yellow circles*, He: *cyan triangles*, O+C: *green squares*, O+Mg: *blue asterisks*, Si: *magenta crosses*, and Fe: *red pluses*). Size of the marks represents the origin of the mass element (the jet: *small*, and the shocked stellar mantle: *large*).

variations of $[C/O]$, $[C/Mg]$, and $[C/Fe]$ corresponds to the variation of $M(\text{Fe})$.

Figure 1d shows that the abundance patterns of EMP stars [20] and HE 1327–2326 with $[Fe/H] = -5.6$ [21, 22] are reproduced by models with $\dot{E}_{\text{dep},51} = 120$ and 1.5, respectively (see Table 1 for model parameters). The model for the EMP stars ejects $M(\text{Fe}) = 0.2M_{\odot}$. On the other hand, the model for HE 1327–2326 ejects $M(\text{Fe}) = 4 \times 10^{-6} M_{\odot}$.

Abundance distribution

Figures 2a and 2b show the abundance distributions at $t = 10^5$ s for models A and B [11]. We classify the mass elements by their abundances as follows: (1) Fe with $X(^{56}\text{Ni}) > 0.04$, (2) Si with $X(^{28}\text{Si}) > 0.08$, (3) O+Mg with $X(^{16}\text{O}) > 0.6$ and $X(^{24}\text{Mg}) > 0.01$, (4) O+C with $X(^{16}\text{O}) > 0.6$ and $X(^{12}\text{C}) > 0.1$, (5) He with $X(^4\text{He}) > 0.7$, and (6) H with $X(^1\text{H}) > 0.3$. If a mass element satisfies two or more conditions, the mass element is classified into the class with the smallest number.

The abundance distribution and thus the composition of the ejecta depend on the direction. In model A, the O+Mg, O+C, He, and H mass elements locate in the all direction. On the other hand, most of the Fe and Si mass elements locate at $\theta < 10^\circ$ and stratify in this order from the jet axis and a part of them locate at $15^\circ < \theta < 35^\circ$. Interestingly, the Fe mass elements surround the Si mass elements at $15^\circ < \theta < 35^\circ$. In model B, most of the O+C and He mass elements locate at $\theta < 3^\circ$, while the Fe mass elements expand laterally up to $\theta = 50^\circ$ and the H mass elements are distributed in the all directions. The lateral expansion of the Fe mass elements in models A and B are led by the collision with the stellar mantle and the internal pressure of the jet.

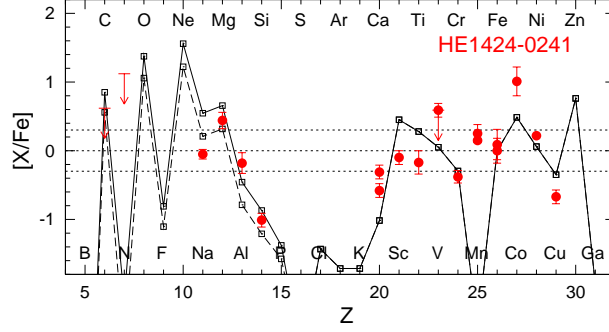


FIGURE 3. Comparison between the abundance pattern of HE 1424–0241 (*filled circles*) and the angle-delimited yields of model A for $30^\circ < \theta < 40^\circ$ (*solid line*) and $30^\circ < \theta < 35^\circ$ (*dashed line*).

A very peculiar, Si-deficient, metal-poor star HE 1424–0241 was observed [23]. Its abundance pattern with high $[\text{Mg}/\text{Si}]$ (~ 1.4) and normal $[\text{Mg}/\text{Fe}]$ (~ 0.4) is difficult to be reproduced by previous SN models. This is because $\log f(X(^{24}\text{Mg})=X(^{28}\text{Si})) = [X(^{24}\text{Mg})=X(^{28}\text{Si})] - \sigma < 1.6$ is realized in the O+Mg layer at the presupernova stage (e.g., [24, 3]). Thus, in order to reproduce the abundance pattern of HE 1424–0241, it is required to consist of explosively-synthesized Fe but not explosively-synthesized Si.

The angle-delimited yield may possibly explain high $[\text{Mg}/\text{Si}]$ and normal $[\text{Mg}/\text{Fe}]$. Figure 3 shows that the yields integrated over $30^\circ < \theta < 40^\circ$ and $30^\circ < \theta < 35^\circ$ of model A reproduce the abundance pattern of HE 1424–0241. The yield consist of Mg in the inner region and Fe in the outer region (Fig. 2a). Although there are some elements to be improved, the elusive feature of HE 1424–0241, high $[\text{Mg}/\text{Si}]$ and normal $[\text{Mg}/\text{Fe}]$, could be explained. The elusive feature can be realized with a model satisfying the following conditions: (a) the Fe mass elements penetrate the stellar mantle (i.e., the duration of the jet injection is long) and (b) the O+Mg mass elements are ejected in all directions (i.e., \dot{E}_{dep} is high).

CONCLUSIONS AND DISCUSSION

We perform two-dimensional hydrodynamical and nucleosynthesis calculations of the jet-induced explosions of a Pop III $40M_\odot$ star and show two jet-induced explosion models A and B as summarized in Table 1. We have shown that (1) the yields of the explosions with high \dot{E}_{dep} explain the abundances of the EMP stars, and (2) the explosions with low \dot{E}_{dep} are responsible for the formation of HE 1327–2326.

(1) **Fallback:** The dynamics and the abundance distributions depend sensitively on \dot{E}_{dep} . The explosion with lower \dot{E}_{dep} leads to a larger amount of fallback, and consequently smaller $M(\text{Fe})$ and higher $[\text{C}/\text{O}]$, $[\text{C}/\text{Mg}]$, and $[\text{C}/\text{Fe}]$. Such dependences of $[\text{C}/\text{Fe}]$ and $M(\text{Fe})$ on \dot{E}_{dep} predict that the higher $[\text{C}/\text{Fe}]$ tends to be realized for lower $[\text{Fe}/\text{H}]$. Note, however, the formation of star with low $[\text{C}/\text{Fe}]$ and $[\text{Fe}/\text{H}]$ is possible because $[\text{Fe}/\text{H}]$ depends not only on $M(\text{Fe})$ but also on the swept-up H mass, i.e., the interaction between the SN ejecta and interstellar matter (ISM) (e.g., [2]).

(2) **Angular dependence:** We present the aspherical abundance distributions and investigate the angular dependence of the yield. The angle-delimited yield could reproduce the extremely peculiar abundance pattern of HE 1424–0241. However, we note that the angle-delimited yield depends strongly on which mass elements are included into the integration. This would be determined by the abundance mixing in the SN ejecta, the interaction between the SN ejecta and ISM, and the region where the next-generation star takes in the metal-enriched gas. It is necessary to calculate three-dimensional evolution of the supernova remnant (e.g., [25]).

ACKNOWLEDGMENTS

This work has been supported in part by World Premier International Research Center Initiative (WPI Initiative), MEXT, Japan, and by the Grant-in-Aid for Scientific Research of the JSPS (18104003, 18540231, 20244035, 20540226) and MEXT (19047004, 20040004). N.T. is supported through the JSPS (Japan Society for the Promotion of Science) Research Fellowship for Young Scientists.

REFERENCES

1. J. Audouze, & J. Silk, *ApJ* **451**, L49–L52 (1995).
2. D. F. Cioffi, C. F. McKee, E. Bertschinger, *ApJ* **334**, 252–265 (1988).
3. H. Umeda, & K. Nomoto, *ApJ* **619**, 427–445 (2005).
4. N. Iwamoto, H. Umeda, N. Tominaga, K. Nomoto, & K. Maeda, *Science* **309**, 451–453 (2005).
5. K. Nomoto, N. Tominaga, H. Umeda, C. Kobayashi, & K. Maeda, *Nucl. Phys. A* **777**, 424–458 (2006).
6. N. Tominaga, H. Umeda, & K. Nomoto, *ApJ* **660**, 516–540 (2007).
7. E. Depagne, et al., *A&A* **390**, 187–198 (2002).
8. M. S. Bessell, & N. Christlieb, “From Lithium to Uranium: Elemental Tracers of Early Cosmic Evolution”, edited by V. Hill, et al., IAU Symposium Proceedings of the international Astronomical Union 228, Cambridge University Press, Cambridge, pp.237–238 (2005).
9. N. Tominaga, et al., *ApJ* **657**, L77–L80 (2007).
10. N. Tominaga, *PhD thesis*, University of Tokyo, (2007).
11. N. Tominaga, *ApJ* in press (arXiv:0711.4815) (2009).
12. W. R. Hix, & F.-K. Thielemann, *ApJ* **460**, 869–894 (1996).
13. W. R. Hix, & F.-K. Thielemann, *ApJ* **511**, 862–875 (1999).
14. I. Hachisu, T. Matsuda, K. Nomoto, & T. Shigeyama, *ApJ* **358**, L57–L61 (1990).
15. K. Maeda, & K. Nomoto, *ApJ* **598**, 1163–1200 (2003).
16. S. E. Woosley, *ApJ* **405**, 273–277 (1993).
17. G. E. Brown, et al. *New Astronomy* **5**, 191–210 (2000).
18. C. Fryer, & P. Mészáros, *ApJ* **588**, L25–L28 (2003).
19. K. Maeda, & N. Tominaga, *MNRAS* submitted (2008).
20. R. Cayrel, et al., *A&A* **416**, 1117–1138 (2004).
21. A. Frebel, et al., *Nature* **434**, 871–873 (2005).
22. W. Aoki, et al., *ApJ* **639**, 897–917 (2006).
23. J. G. Cohen, et al., *ApJ* **659**, L161–L164 (2007).
24. S. E. Woosley, & T. A. Weaver, *ApJS* **101**, 181–235 (1995).
25. N. Nakasato, & T. Shigeyama, *ApJ* **541**, L59–L62 (2000).